A&A 603, A123 (2017)
DOI: 10.1051/0004-6361/201629696

Astronomy & Astrophysics

Dust in brown dwarfs and extrasolar planets

V. Cloud formation in carbon- and oxygen-rich environments

Ch. Helling, D. Tootill, P. Woitke, and G. Lee

Centre for Exoplanet Science, SUPA, School of Physics and Astronomy, University of St. Andrews, North Haugh, St. Andrews, Fife, KY16 9SS, UK
e-mail: ch80@st-and.ac.uk

Received 12 September 2016 / Accepted 6 December 2016

ABSTRACT

Context. Recent observations indicate potentially carbon-rich (C/O > 1) exoplanet atmospheres. Spectral fitting methods for brown dwarfs and exoplanets have invoked the C/O ratio as additional parameter but carbon-rich cloud formation modeling is a challenge for the models applied. The determination of the habitable zone for exoplanets requires the treatment of cloud formation in chemically different regimes.

Aims. We aim to model cloud formation processes for carbon-rich exoplanetary atmospheres. Disk models show that carbon-rich or near-carbon-rich niches may emerge and cool carbon planets may trace these particular stages of planetary evolution.

Methods. We extended our kinetic cloud formation model by including carbon seed formation and the formation of C[s], TiC[s], SiC[s], KCl[s], and MgS[s] by gas-surface reactions. We solved a system of dust moment equations and element conservation for a prescribed DRIFT-PHOENIX atmosphere structure to study how a cloud structure would change with changing initial C/O_0 = 0.43 . . . 10.0.

Results. The seed formation efficiency is lower in carbon-rich atmospheres than in oxygen-rich gases because carbon is a very effective growth species. The consequence is that fewer particles make up a cloud if $C/O_0 > 1$. The cloud particles are smaller in size than in an oxygen-rich atmosphere. An increasing initial C/O ratio does not revert this trend because a much greater abundance of condensible gas species exists in a carbon-rich environment. Cloud particles are generally made of a mix of materials: carbon dominates if $C/O_0 > 1$ and silicates dominate if $C/O_0 < 1$. A carbon content of 80–90% carbon is reached only in extreme cases where $C/O_0 = 3.0$ or 10.0.

Conclusions. Carbon-rich atmospheres form clouds that are made of particles of height-dependent mixed compositions, sizes and numbers. The remaining gas phase is far less depleted than in an oxygen-rich atmosphere. Typical tracer molecules are HCN and C_2H_2 in combination with a featureless, smooth continuum due to a carbonaceous cloud cover, unless the cloud particles become crystalline.

Key words. astrobiology – astrochemistry – planets and satellites: gaseous planets – planets and satellites: atmospheres – methods: numerical

1. Introduction

Spectral observations of extrasolar planets reveal their chemical content which is linked to the planet's formation process but which is altered by planetary evolution. Migration and disk evolution, however, may challenge the direct and easy linking of present-day observable composition and planet formation. A couple of observations point to the possibility of planets with carbon-rich atmospheres. Madhusudhan et al. (2011) suggested the WASP-12b has a carbon-rich atmosphere based on a day-side emission spectrum, even though its host star is oxygen-rich. This is based on a synthetic spectrum comparison derived for a parameterized atmosphere structure to fit the observations. Kreidberg et al. (2015) have retrieved the presence of H_2O with a $C/O \approx 0.5$ on the dayside of the planet from the *Hubble* Space Telescope (HST) transmission spectrum of WASP-12b, and these authors suggest an atmosphere with clouds and haze and absorption by, for example, CO, CH_4, HCN, C_2H_2 and FeH. The planets HD 8988b,c,d,e have been tentatively suggested to show molecules (b & d: CH_4, C_2H_2, CO_2; c: C_2H_2; e: CH_4, C_2H_2; Oppenheimer et al. 2013) typical for carbon-rich atmospheres (Helling et al. 1996). Tsiaras et al. (2016) analyze WFC3 HST data for the super-Earth 55 Cancri e and derive a C/O = 1.1 on this evaporating, probably hydrogen-rich planet and suggest a tentative HCN detection. Jura et al. (2015) report on a polluted Keck/HIRES spectrum of the white dwarfs WD Ton 345 that suggest that the accreted disk planetisimals (debris of a disrupted planet) must have been carbon rich and water poor.

Disk chemistry simulations suggest that local disk gas can become carbon rich but only under special circumstances and at certain times (Helling et al. 2014; Ali-Dib et al. 2014; Eistrup et al. 2016). This suggests that carbon-rich planets could be a tracer of these rare episodes in an originally oxygen-rich disk. When planets form by the core-accretion scenario, smaller planetary masses would favor an enrichment with heavy elements inside the core.

The dominatant sources of carbon (and Al and Li) in the universe are evolved stars that undergo the third dredge up on the asymptotic giant branch. Dust-driven winds (radiation pressure due to large luminosities) then enrich the interstellar medium (ISM) with these elements. Abia et al. (2003) show that solar-metallicity AGB stars with C/O ~ 1 and a C/O > 2 are considered extreme. Nuclear synthesis and evolutionary models show

that only low-metallicity AGB stars would produce C/O = 10 (Abia et al. 2003). Given the low abundance of carbon-rich, nearly-sun-like stars (Fortney 2012), carbon-rich planets around those stars most likely must be linked to the disk evolution rather than to a primordial C/O > 1. The situation may differ for planets around carbon-rich AGB stars, which may well have been enriched by the dust that leaves the star in abundance during its wind phases with mass losses of $10^{-7} \ldots 10^{-4}\ M_{\odot}\,\mathrm{yr}^{-1}$ (e.g. Schröder et al. 1998; Winters et al. 2003). The dominating sources for carbon in the early universe, however, are Population III SNe ejecta. Carbon-rich planets could now form in situ as by-products of carbon-enhanced metal-poor stars (CEMPs), i.e., carbon-rich Pop II stars, as suggested by Mashian & Loeb (2016). Would such planets still have clouds? First investigations of metal-deficient ultra-cool atmospheres were carried out only for oxygen-rich gases only but demonstrated that cloud do prevail to unexpected low metallicities of [M/H] ≈ –5.0 (Witte et al. 2009).

Linking spectra of extrasolar planets to planet formation and disk evolution,therefore, requires the possibility of treating oxygen-rich and carbon-rich atmospheres and the chemical transition from one to the other. An essential part of this task is to be able to treat cloud formation in such chemically diverse environments. Also determining the habitable zone for extrasolar planets demands detailed cloud models across various chemical regimes (Yang et al. 2013; Barnes et al. 2016).

We present results from a kinetic cloud formation model treating seed formation, growth/evaporation, gravitational settling and element depletion to form cloud particles of height-dependent, mixed compositions and size in carbon-rich and oxygen-rich environments. We present first results from our next generation of cloud formation models, which follow the moment approach presented in Woitke & Helling (2003, 2004), Helling & Woitke (2006), Helling et al. (2008). Section 2 summarizes our approach. Section 3 presents our results for clouds in atmospheric environments of changing C/O ratios from C/O < 1 (oxygen rich) to C/O > 1 (carbon rich), and presents how global cloud properties change with evolving C/O. One of the questions to be answered is under which conditions cloud particles would form primarily (>80%) of pure carbon. Sections 4 and 5 present the results for the remaining gas-phase elements and discuss some example molecules, respectively. Section 6 summarizes this paper.

2. Approach

We present a new generation of our kinetic, nonequilibrium cloud formation model, which allows us to investigate cloud structures in oxygen-rich and carbon-rich environments and the transition between the two. We assess the impact of the carbon-to-oxygen ratio (C/O) on the resulting cloud structure details for giant gas planet atmospheres. We utilize example model atmosphere structures ($T_{\rm eff}$ = 1600 K and 2000 K, log(g) = 3.0, initial solar metallicity) from the Drift-PHOENIX atmosphere grid that is representative for the atmosphere of a giant gas planet. We use the model ($T_{\rm gas}$, $p_{\rm gas}$)-structure as input for our external cloud formation program DRIFT to derive the cloud structures details for different C/O ratios by adjusting the carbon abdundance. All other elements are kept at solar values. We present our results for a selected set of C/O ratios (0.43, 1.0, 1.1, 1.5). We assume that the planets form via the core-accretion scenario and that the accreted dust has already settled out and leaves behind an atmosphere with the respective C/O ratio.

2.1. Cloud formation model

Our cloud formation model describes the formation of clouds by nucleation, subsequent growth by chemical surface reactions on-top of the seeds, evaporation, gravitational settling, element conservation and convective replenishment (Woitke & Helling 2003, 2004; Helling & Woitke 2006; Helling et al. 2008; for a summary see Helling & Fomins 2013). The effect of nucleation, growth and evaporation on the remaining elements in the gas phase is fully accounted for (Eqs. (10) in Helling et al. 2008). The surface growth of a diversity of materials causes the cloud particles to grow to μm-sized particles of a mixed composition of those solids taken into account. Cloud particles size and material composition change with height in the atmosphere.

We extended our model to enable a simultaneous treatment of multiple nucleation species (seed formation) and to allow for the formation and growth of mixes of carbonaceous and silicate materials. The above references provide the formula body of our cloud formation model.

Seed formation: the seed formation is described by classical nucleation theory, which has been modified for TiO_2 nucleation to take knowledge about $(TiO_2)_N$ cluster formation into account (Jeong et al. 1999, 2000; Lee et al. 2015). We follow the approach, including all material constants, as described in Lee et al. (2015) for TiO_2 seed formation.

The second seed formation species that we take into account is carbon. We do not present any new development of carbon nucleation but apply the approach used for AGB star wind modeling, for example in Fleischer et al. 1992; Woitke 2006, but for the more complete gas-phase chemistry described in Bilger et al. (2013).

In an oxygen-rich gas (C/O = 0.43), we only apply TiO_2 nucleation as all carbon is blocked in CO or CH_4. In a clearly carbon-rich case (C/O = 1.1, 1.5, 3.0, 10.0), we apply only carbon nucleation as all oxygen is locked up in CO. We demonstrate in Sect. 3.1.1 the simultaneous treatment of TiO_2 and C nucleation for the case C/O = 1.0 where the required oxygen and carbon are not blocked by CO, and the gas-phase composition becomes substantially more demanding.

Surface growth: the growth of the cloud particle bulk is described by gas-surface reactions between the gas and cloud particle surface as described in Helling & Woitke (2006) and Helling et al. (2008). As different materials can become thermally stable at very similar temperatures, a mix of materials grows. The surface reactions that were used are summarized in Tables A.3 and A.2. For carbon-rich cases, we apply the set of surface reactions listed in Table A.3, and for oxygen-rich cases Table A.2. The chemical transition case of equal carbon and oxygen abundances (C/O = 1.0) is represented by Table A.2 with the addition of C[s], SiC[s], TiC[s], KCl[s] and MgS[s] from Table A.3. The vapor pressure data used for the materials that were added to our cloud model (C[s], MgS[s], TiC[s], SiC[s] and KCl[s]) are given in Table A.1.

2.2. Drift-Phoenix model atmosphere

DRIFT-PHOENIX (Dehn 2007; Helling et al. 2008; Witte et al. 2009) model atmosphere simulations solve the classical 1D model atmosphere problem coupled to a kinetic phase-nonequilibrium cloud formation model. Each of the model atmospheres is determined by the effective temperature ($T_{\rm eff}$ [K]),

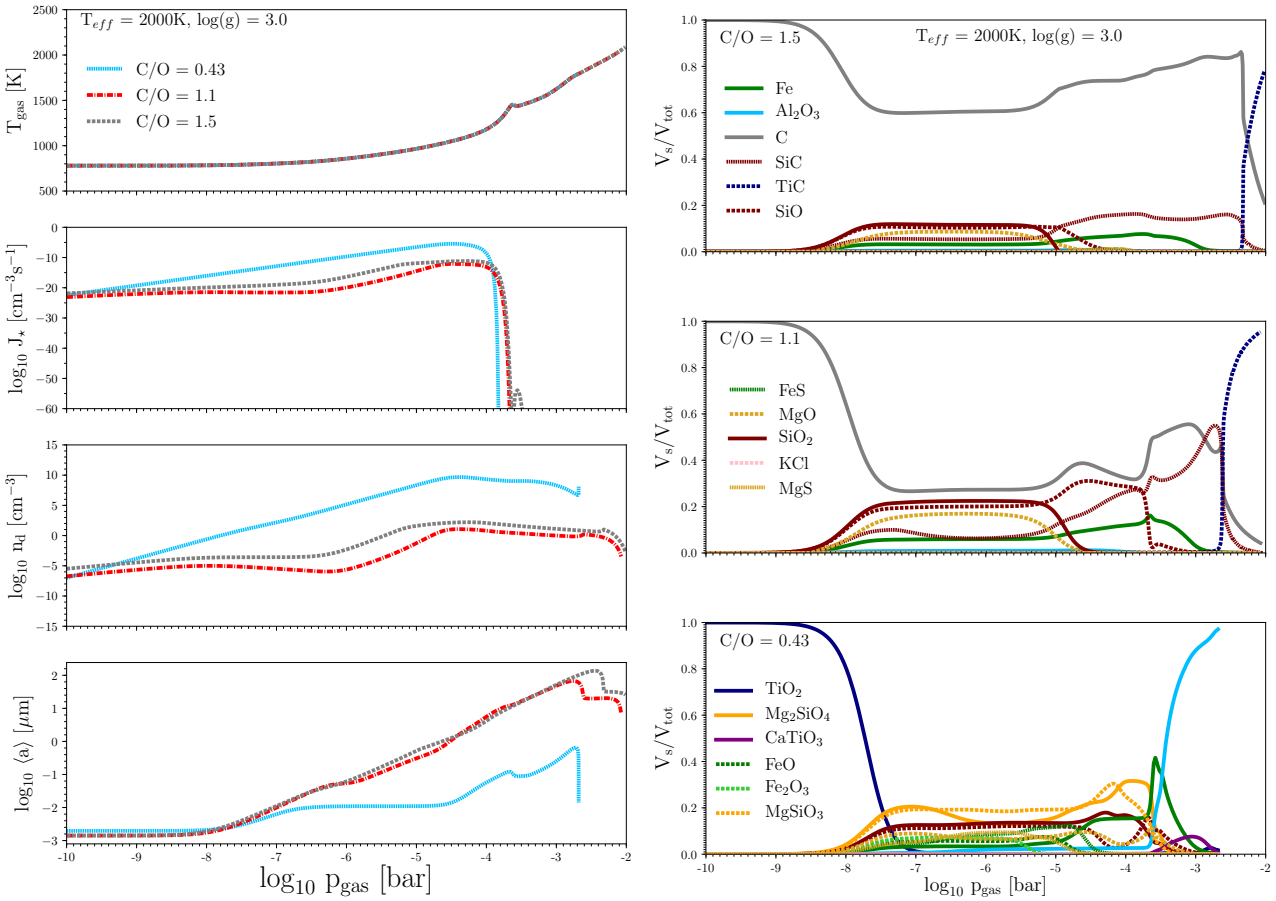

Fig. 1. *Left*: cloud structures for changing C/O = 0.43 (blue), 1.1 (red), 1.5 (gray) for a prescribed DRIFT-PHOENIX ($T_{\rm gas}$, $p_{\rm gas}$) structure for a giant gas planet with $T_{\rm eff}$ = 2000 K, log(g) = 3.0, initial solar element abundances. *1st panel*: input $T_{\rm gas}$ [K] and $p_{\rm gas}$ [bar], *2nd panel*: nucleation rate log J_* [cm^{-3} s^{-1}], *3rd panel*: cloud particle number density log $n_{\rm d}$ [cm^{-3}], and *4th panel*: mean cloud particle radius log$\langle a \rangle$ [μm]. *Right*: changing material composition, $V_s/V_{\rm tot}$ [%] (relative volume fractions of solid species s) of the cloud particles with changing C/O ratio.

surface gravity (log(g) (with g in cm/s^2)), and element abundances. The opacity of the cloud is calculated by applying Mie and effective medium theory.

The 1D atmosphere models provide atmospheric properties such as the local convective velocity and the temperature-pressure ($T_{\rm gas}$ [K], $p_{\rm gas}$ [dyn/cm^2]) structure. The local temperature is the result of the radiative transfer solution, the local gas pressure of the hydrostatic equilibrium. For lack of a consistent solution as of yet, we applied the same oxygen-rich atmosphere structure in all tests presented in this paper.

3. Clouds in atmospheric environments of changing C/O ratio from C/O < 1 to C/O > 1

3.1. Changing cloud structures with changing C/O

The cloud structure of oxygen-rich giant gas planets and brown dwarfs is well understood based on kinetic cloud modeling (Helling & Fomins 2013; Helling & Casewell 2014), but this cloud structure still depends on the basic material constants (e.g. vapor pressure and cluster data; Fortney et al. 2016) and poses a challenge as part of atmosphere model simulations (forward and retrieval), in which it is most often parameterized. In a stationary scenario, haze-like small cloud particles comprised of a rich mix of silicates and metal-oxides populate the uppermost cloud layers. If they precipitated through the atmosphere, the cloud particles change their size and the material composition becomes dominated by Mg/Si/O materials with only small inclusions from iron and other oxides. The innermost cloud region is made of big particles with a mix of high-temperature condensates of which one is always dominating (e.g., TiO_2[s] or Fe[s]). This is the case for C/O = 0.43, which is shown for reference in Fig. B.1 (right). This cloud structure is a refinement of the DRIFT-PHOENIX result as published in Witte et al. (2009).

Over-all cloud structure: Fig. 1 (left) demonstrates how the cloud structure changes if the initial C/O ratio (C/O$_0$) changes from an oxygen-rich (C/O$_0$ < 1) to a carbon-rich (C/O$_0$ > 1) gas-composition. Such a drastic change in environmental chemistry can occur during disk evolution and also because of the set-in of dust formation (Helling et al. 2014). We present our results for C/O$_0$ = 0.43 (blue), 1.1 (red), and 1.5 (gray). Figure 1 (right) shows how the material composition of the cloud particles (in units of $V_s/V_{\rm tot}$ – relative volume fractions of solid species s) change.

The results from the second panel in Fig. 1 (left) show that the nucleation rate of TiO_2 (light blue line) in an oxygen-rich environment exceed that of C in a carbon-rich gas (red line) because carbon is initially considerably more abundant in the gas phase and therefore grows very quickly onto the newly formed grain. This leads to a rapid decrease of carbon in the gas, which causes the nucleation process to stop. An increase in C/O ratio to C/O$_0$ = 1.5, i.e., an increase of carbon, leads to a

somewhat increased seed formation rate (gray) compared to the $C/O_0 = 1.1$ case.

A larger nucleation rate leads to more seeds forming and hence a larger number density of cloud particles n_d (Fig. 1, left, 3rd panel) for a given (T_{gas}, p_{gas}) structure. The nucleation rates reach their maximum at almost the same pressure level independent of the initial C/O ratio. This might change if carbon-cloud and temperature structure were consistently treated. The cloud extends below the nucleation regimes in all cases depicted in Fig. 1 (left, compare 2nd and 3rd panel) as the growing cloud particles gravitationally settle into deeper atmospheric layers.

The bottom panel of Fig. 1 (left) shows that the large number of seeds in the oxygen-rich case results in the smallest average cloud particles sizes, as now more surface area is available onto which a given number of gas species grows. As a result the cloud particles in a carbon rich environment are larger but less numerous. The average particle size of cloud particles in carbon-rich environments does not appear to differ drastically between just carbon-rich environments and more concentrated carbon-rich environments, even though the latter has a higher number density by as much as three orders of magnitude in places. This suggests that there exists a much greater abundance of potential condensible gas species in a rich carbon environment, such that the increased number density is canceled out.

Cloud composition: Figure 1 (right; see also Fig. B.1 for comparison in more detail) presents what materials the cloud particles are made of, how their composition changes with height, and how it changes with changing C/O_0 ratio. The plotted values, V_s/V_{tot}, are the relative volume fractions of the solid s and are calculated from Eqs. (3) in Helling et al. (2008). Of particular interest is the question of whether cloud particles in a carbon-rich atmosphere will remain homogeneous as commonly assumed for AGB star wind modeling (Fleischer et al. 1992; Mattsson et al. 2010; Wittkowski et al. 2016), or if they are composed of some mix of materials similar to the chemically more complex oxygen-rich case.

In a heavily carbon-rich atmosphere (here: $C/O_0 = 1.5$), the dominant dust component is C[s], with it making up at least 60% of the volume except for at the deepest atmospheric layers, where TiC[s] becomes more prevalent. The top panel in Fig. 1 (right) also shows the emergence of SiC[s] in the inner atmosphere, where it becomes the second most abundant material between 10^{-5} bars and roughly $10^{-3.5}$ bars. Other significant components of the dust phase in the mid-atmosphere are SiO[s], SiO_2[s], and MgO[s], reaching a volume fraction of ≈30%. Fe[s] appears in small amounts that increase somewhat when SiO[s], SiO_2[s], and MgO[s] have evaporated.

In comparison, a carbon-rich atmosphere at a lower C/O ratio (here: $C/O_0 = 1.1$), carbon, while still the most abundant dust component for most of the cloud layer, comprises as little as 30% of the dust volume once other materials begin to condense onto the cloud particles. The proportional increase of oxygen aids the condensation of oxygen bearing dust species, such as SiO[s], SiO_2[s] and MgO[s] in the mid-cloud layer. SiO[s] exists for roughly an extra bar of pressure in depth compared to $C/O_0 = 1.5$. The abundance of SiC[s] also increases to a maximum of ≈50% of the dust volume at its peak, compared to just 20% for a $C/O_0 = 1.5$. Also, Fe[s] has increased its volume fraction to as much as 10...15%.

In an oxygen-rich environment (here: $C/O_0 = 0.43$) the seed particle TiO_2 is the prevalent species only during the nucleation period, in the upper-most cloud layers where dust growth does not occur efficiently. Once condensation onto the seed particles begins the dust volume instead comprises of a mixture of Mg_2SiO_4[s], $MgSiO_3$[s] and many other silicate and oxide species.

To summarize, the seed particle material comprises a much more significant fraction of the total dust volume in carbon-rich cases because of the higher elemental abundances of C compared to Ti. In both environments, silicon species seem to form a large portion of the dust, bonded to Mg and multiple O in the oxygen-rich environments, and simply O or O_2 in the carbon-rich environments.

3.1.1. The case of $C/O_0 = 1.0$

Disk evolution seems to suggest that a chemical situation in which $C/O \approx 1$ is not uncommon. ProDiMo[1] (Woitke et al. 2009, 2016) chemical disk model results presented in Helling et al. (2014) suggest that at 10 Myr a $C/O \approx 1.0$ range appears between 1... 10 AU. While the exact number depends on the model setup (and on the chemical rates applied), the $C/O \approx 1.0$-range may well be a common feature during certain evolutionary disk stages, or could even be indicative of this feature. Assuming that the disk dust has settled onto/into the planet core and that the planet is cold enough that no outgassing occurs, the planet is then left with a $C/O \approx 1.0$ atmosphere. Hence, an evolving planet has to go through this stage of evolution at some point in its lifetime. Here we use our cloud formation model to study the cloud details that occur should a planet be affected by the external disk $C/O \approx 1$ or otherwise achieve $C/O \approx 1$.

Modeling cloud formation in an atmosphere in which carbon and oxygen appear in the same amounts and are locked up in CO is challenging because none of the well-studied cases (oxygen rich and carbon rich) can be used as guide. While it is not obvious which nucleation species to use (with the added challenge of the availability of material data), we use the case to perform some tests on the effect of the nucleation species on a potentially forming cloud. To do so, we perform three test: i) TiO_2 nucleation only; ii) carbon nucleation only,; and iii) simultaneous carbon and TiO_2 nucleation. All three test calculations use the same set of surface growth reactions in Table A.2 with the addition of C[s], SiC[s], TiC[s], KCl[s], and MgS[s] from Table A.3. Hence, the only difference is how we treat the formation of seed particles.

Figure 2 shows how the different nucleation species affect the overall cloud structure. The pure carbon nucleation is the least efficient seed formation process in the case of $C/O = 1.0$, and pure TiO_2 nucleation is the most efficient. The result is that pure carbon-seeds would lead to very few cloud particles (Fig. 2, left, 3rd panel, red dashed lines) as it occurs with 10 order of magnitudes less efficiency (2nd panel, red dashed lines). It might, however, be unexpected that the mean cloud particle radii (Fig. 2, left, 4th panel) do not differ by too much. Figure 2 (right) demonstrates the material mix that can be expected for cloud particles forming from a gas of initially $C/O = 1$. While the upper cloud deck is dominated by the seed forming species material, the remaining cloud where the surface growth causes the largest increase in grain size, is rather similar between the three cases shown in Fig. 2. Given that the nucleation process determines the whole cloud structure we suggest using carbon and TiO_2-nucleation to optimally represent the cloud structure in an atmosphere where $C/O \approx 1$. The details of the material

[1] Radiation thermochemical models of protoplanetary disks.

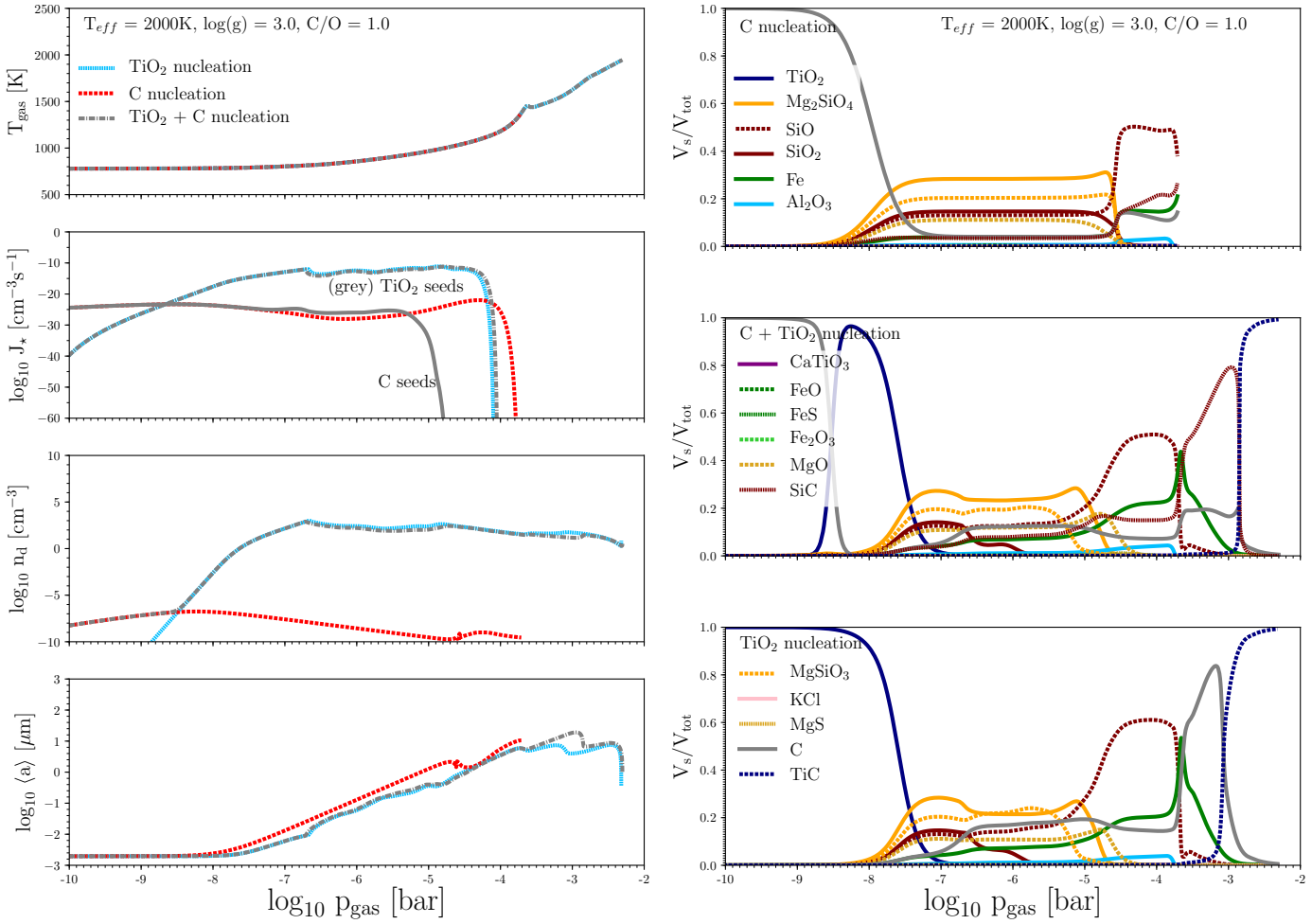

Fig. 2. Clouds formation at C/O = 1.0 for a prescribed DRIFT-PHOENIX ($T_{\rm gas}$, $p_{\rm gas}$) structure for a giant gas planet with $T_{\rm eff}$ = 2000 K, log(g) = 3.0, initial solar element abundances. Three cases are tested: i) TiO_2 nucleation only (light blue); ii) carbon nucleation alone (red); and iii) simultaneous carbon and TiO_2 nucleation (gray). *Left*: *1st panel*: input $T_{\rm gas}$ [K] and $p_{\rm gas}$ [bar], *2nd panel*: nucleation rate log J_* [cm^{-3} s^{-1}], *3rd panel*: cloud particle number density log $n_{\rm d}$ [cm^{-3}], and *4th panel*: mean cloud particle radius log$\langle a \rangle$ [μm]. *Right*: changing material composition, $V_{\rm s}/V_{\rm tot}$ [%] (relative volume fractions of solid species s) of the cloud particles for different nucleation species.

composition is discussed as part of our study of varying C/O in Sect. 3.3.

3.2. Decreasing $T_{\rm eff}$

Given the strong temperature dependence on cloud formation processes and, in particular, on seed formation (see steep gradient of J_* in, e.g., Figs. 1, 2), we examine the impact of decreasing $T_{\rm eff}$ of the atmosphere from 2000 K to 1600 K on the cloud structure and composition. The surface gravity remains the same at log(g) = 3.0 and initial solar element abundances for C/O$_0$ = 0.43, 1.1, 1.5 are studied.

Cloud structure: Figure 3 shows for $T_{\rm eff}$ = 1600 K (log(g) = 3.0); the changes in the cloud structure move from the oxygen-rich environment (C/O$_0$ = 0.43) to carbon-rich cases (C/O$_0$ = 1.1, 1.5). As for the previous case, the nucleation rate of TiO_2 (second panel, blue) in the oxygen rich case is greater than that of the carbon nucleation in either carbon rich atmosphere. Compared to $T_{\rm eff}$ = 2000 K (Fig. 1) the nucleation rate is lower for all C/O ratios, but is particularly pronounced in mid cloud-layer (10^{-7} to 10^{-5} bars) in the carbon-rich environments where a dip in the nucleation rates of carbon seeds is observed. The nucleation rate is on the order of 10 (C/O$_0$ = 1.5) to 20 (C/O$_0$ = 1.1) magnitudes smaller. Nucleation of seed particles also continues for roughly a bar in depth deeper for all C/O regimes, compared with $T_{\rm eff}$ = 2000 K.

The lower nucleation rates have a dramatic impact on the number density of cloud particles, particularly in the carbon-rich cases. For the oxygen-rich environment, there is a four order decrease in magnitude in the number density of cloud particles at the top of the cloud level at $T_{\rm eff}$ = 1600 K compared to $T_{\rm eff}$ = 2000 K, however, this difference becomes negligible deeper into the cloud structure. The number density increases at 10^{-5} bars (in the present model) for C/O$_0$ = 1.5 and 10^{-4} bars for C/O$_0$ = 1.1 due to increasing nucleation rates, which are more sharply pronounced than the slight increase present for $T_{\rm eff}$ = 2000 K. The minor decrease in number density in the carbon-rich regimes between 10^{-8} bars and $10^{-5}/10^{-4}$ bars is from greater gravitational settling, which is due to the increased grain size, that causes more cloud particles to rain out to lower cloud levels than new seeds can replace.

As is expected, the average grain size (4th panel, Figs. 1, 3) remains much smaller in the oxygen-rich environments, where

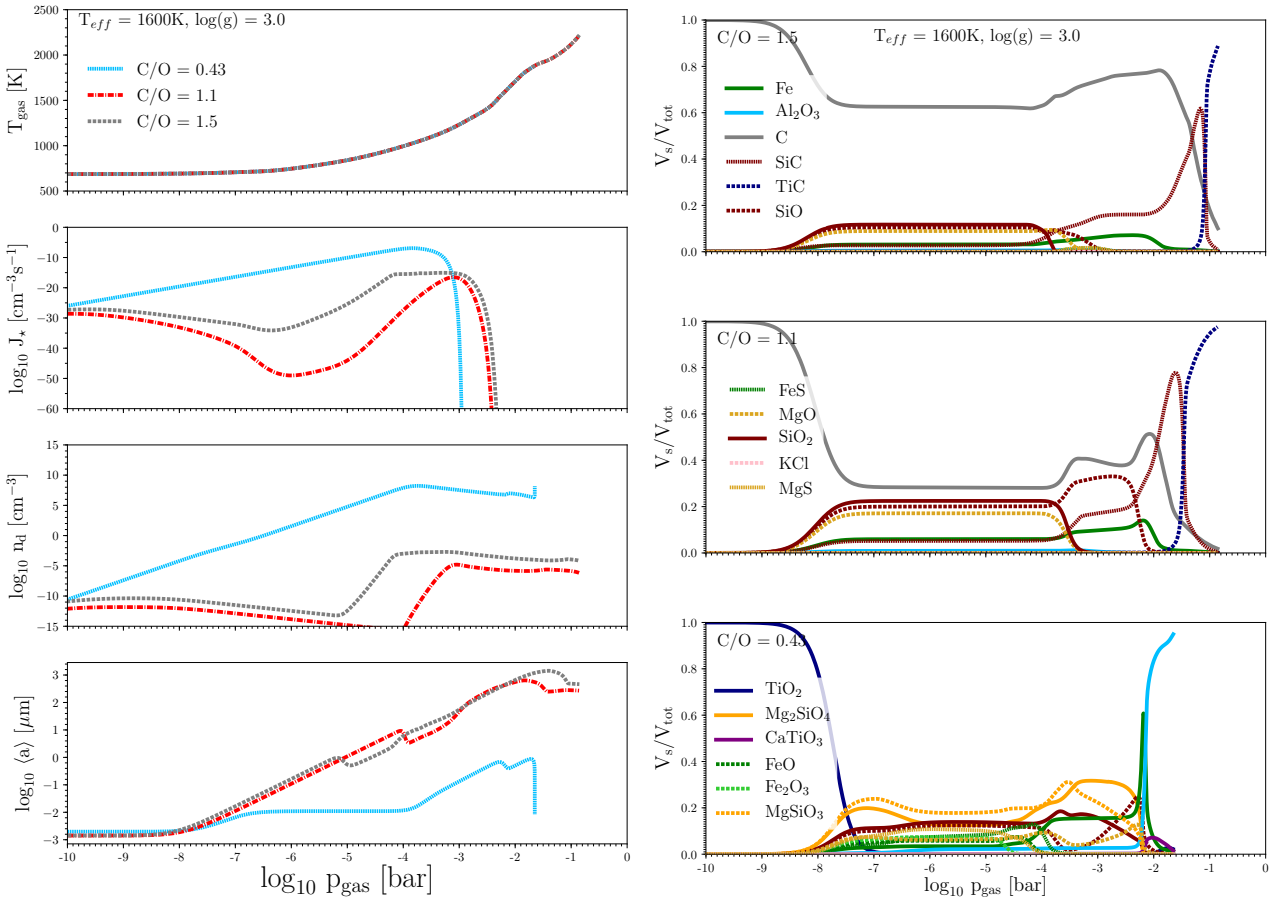

Fig. 3. Cloud structures for changing C/O = 0.43 (blue), 1.1 (red), and 1.5 (gray) for a prescribed DRIFT-PHOENIX ($T_{\rm gas}$, $p_{\rm gas}$) structure for a giant gas planet with $T_{\rm eff}$ = 1600 K, log(g) = 3.0, initial solar element abundances. *Left*: *1st panel*: input $T_{\rm gas}$ [K] and $p_{\rm gas}$ [bar], *2nd panel*: nucleation rate log J_* [cm^{-3} s^{-1}], *3rd panel*: cloud particle number density log $n_{\rm d}$ [cm^{-3}], and *4th panel*: mean cloud particle radius log$\langle a \rangle$ [μm]. *Right*: changing material composition, $V_s/V_{\rm tot}$ [%] (relative volume fractions of solid species s), of the cloud particles for different nucleation species.

there is extra competition for condensible material between the more numerous cloud particles than for carbon-rich environments. Additionally, given the vastly lower number density of cloud particles in an atmosphere with $T_{\rm eff}$ = 1600 K, the cloud particles grow to much larger radii than in the $T_{\rm eff}$ = 2000 K case. At the lower cloud levels, the average grain size is an order of magnitude greater than for $T_{\rm eff}$ = 2000 K. As in the hotter environment, however, the average grain size remains largely independent of the degree of carbon abundance.

Cloud composition: Figure 3 shows the composition of the cloud particles throughout the cloud level. There is no change at the top of the cloud level with all the dust comprising of seed particle material. As in the $T_{\rm eff}$ = 2000 K atmosphere there is a more significant decrease in the carbon fraction of the dust for the less carbon-rich case. The condensation of other growth species again begins roughly 10^{-8} bars with silicate and magnesium compounds comprising the largest noncarbon fractions of the dust (SiO[s], SiO_2[s], and MgO[s] for C/O$_0$ > 1; Mg_2SiO_4[s], $MgSiO_3$[s], and SiO_2[s] for C/O$_0$ < 1).

The composition of the dust in the bulk of the cloud structure, from 10^{-8} bars to 10^{-3} bars, remains largely unchanged upon altering $T_{\rm eff}$. The analysis of the differences between a carbon-rich cloud composition and oxygen-rich cloud composition presented in Sect. 3.1, hold in this region as well.

Changes in the cloud composition appear deep within the cloud layer. In the oxygen-rich environment there is a larger spike in the volume fraction of Fe[s] prior to the sharp increase of Al_2O_3[s] which then becomes the dominant fraction. In the carbon-rich environments SiC[s] becomes a major constituent of the dust volume, which is roughly 70% for C/O$_0$ = 1.5 and 80% at C/O$_0$ = 1.1. This compares to a maximum of roughly 15% for C/O$_0$ = 1.5 and 60% for C/O$_0$ = 1.1 for $T_{\rm eff}$ = 2000 K. The SiC[s] in the dust replaces pure carbon suggesting that for cooler effective temperatures the deep cloud layers become richer in Si-binding species.

3.3. Global changes of cloud properties with changing C/O$_0$, including the extreme

We demonstrate how the globally changing C/O ratio effects global cloud properties. This may be envisioned as an evolutionary C/O sequence from a typical oxygen-rich to a strongly carbon-rich environment. Two scenarios may be envisisoned for such an evolutionary C/O sequence: first, an AGB star enriching the planet when it evolved away from the main sequence and, second, a planet encountering chemically different accretion environemnts in a planet-forming disk. In this first study, we wish to derive global cloud trends for changing C/O ratios. We therefore also consider extreme values (C/O$_0$ = 3.0 and 10.0), which are guided by observations of carbon-rich Pop II stars

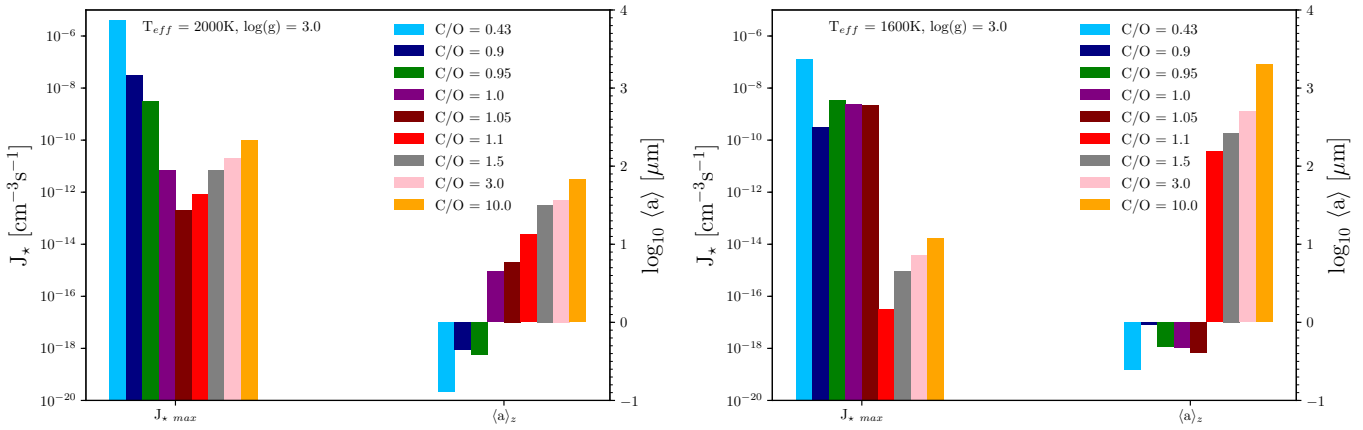

Fig. 4. Global changes of cloud structure. Changes in maximum nucleation rate throughout cloud layer (left cluster of bars) and average mean grain size throughout cloud layer (right cluster of bars). Data taken from range of C/O$_0$ ratios from 0.43 to 10.0. *Left*: $T_{\rm eff}$ = 2000 K and log(g) = 3.0. *Right*: $T_{\rm eff}$ = 1600 K and log(g) = 3.0.

(e.g., Table 1 in Mashian & Loeb 2016 and references therein). The results are summarized in Table 1 and in Fig. 4.

Three C/O-regimes are considered: the oxygen-rich regime (C/O$_0$ = 0.43 and 0.9), the transition regime (C/O$_0$ = 0.95, 1.0 and 1.05) and the carbon-rich regime (C/O$_0$ = 1.1, 1.5, 3.0 and 10.0). The oxygen- and carbon-rich cases were treated with a single seed species (TiO$_2$ and C, respectively) as described in Sect. 2.1. The transition region was treated with both seed species and an increased selection of growth species as described in Sect. 3.1.1.

We utilize the following properties to provide a global characterization of the cloud: the maximum nucleation rate, $J_{*,\rm max}$ [cm^{-3} s^{-1}], the average mean cloud particle size $\langle a\rangle_{\rm avg}$ [μm] (mean cloud particle radius, $\langle a\rangle$, averaged over whole vertical, 1D cloud extension), and three characteristic values for the cloud particles material composition (top, middle, and bottom of cloud).

Maximum nucleation rate: the maximum nucleation rate, $J_{*,\rm max}$, within the cloud structure (left cluster of bars in Fig. 4) decreases as the initial C/O ratio approaches unity from the oxygen-rich side. This is due to the decrease in oxygen that is not locked up in CO resulting in a gas-phase abundance of TiO$_2$ that forms seed particles. The maximum nucleation rate then increases again as the initial C/O increases above unity, again from the increased abundance of gas-phase seed material, in this case, carbon. The maximum nucleation rate can be greater at unity than at C/O$_0$ = 1.05 because of the greater availability of TiO$_2$ in the gas phase with which to form seeds. TiO$_2$ is a more efficient seed forming species than C, which results in higher maximum nucleation rates even if the gas-phase abundance of carbon is much greater (such as in the extreme C/O$_0$ = 10 compared with the slightly oxygen-rich environment of C/O$_0$ = 0.9). This trend is also present for $T_{\rm eff}$ = 1600 K (Fig. 4 right), although it is less pronounced in the transition regime (C/O$_0$ = 0.95, 1.0, and 1.05).

Average mean cloud particle size: the average mean grain size, $\langle a\rangle_{\rm avg}$, across the whole cloud layer (right cluster of bars on Fig. 4) shows an increasing trend with increasing global C/O$_0$. From previous sections, it was anticipated that the cloud particles present in the carbon-rich atmosphere would be larger than those in the oxygen-rich atmosphere, because of the decreased competition for condensible growth material as a result of fewer seed particles forming. The increase in the averaged mean grain size, $\langle a\rangle_{\rm avg}$, as the initial C/O ratio increases in the oxygen-rich regime is also cause by lower number densities of seed particles. The increasing average mean particle size, $\langle a\rangle_{\rm avg}$, with increasing initial C/O ratio in the carbon-rich regime, however, may not be explained by this reasoning as the nucleation rate also increases as the initial C/O ratio increases. Therefore, the increased $\langle a\rangle_{\rm avg}$ are instead the result of increased availability of growth material, specifically with regards to carbon as a growth species. This is a conjecture supported by the high proportion of carbon present in the dust composition of cloud particles at almost every part of the cloud layer, as presented in the top two panels of Fig. 1 (right).

Dust composition: the upper level of the cloud layer for every initial C/O ratio is made of the respective seed material. For the transition regime (C/O$_0$ = 0.95, 1.0, and 1.05), the C/O ratio decides which seed condenses first with C/O < 1 producing TiO$_2$ seeds and C/O>= 1 producing carbon seeds. The cloud particle volume in the middle of the cloud layer is made of numerous materials. In the oxygen-rich and transition regimes the largest volume fractions consist of Mg$_2$SiO$_4$[s], MgSiO$_3$[s], SiO[s], and SiO$_2$[s]. The percentage of Mg$_2$SiO$_4$[s] grows slightly as the C/O$_0$ increases with the small fraction of Al$_2$O$_3$[s] present at C/O$_0$ = 0.43 becoming negligible as the C/O$_0$ ratio increases. In contrast, the largest components of the normal carbon-rich environments (C/O$_0$ = 1.1 and 1.5) replace the fractions of Mg$_2$SiO$_4$[s] and MgSiO$_3$[s] with larger proportions of SiO[s], SiO$_2$[s], and MgO[s] as well as C[s]. As the C/O$_0$ ratio increases, the fraction of C[s] increases as well at the expense of SiO[s], SiO$_2$[s] and MgO[s]. This trend is continued to the extreme C/O$_0$ ratios of 3.0 and 10.0 where the dust volume at the middle of the cloud layer is almost completely comprised of carbon. At the bottom of the cloud layer more stable dust species such as Al$_2$O$_3$[s] dominate in the oxygen-rich regime, although with volume fractions that decrease as the C/O$_0$ ratio increase with increasing fractions of Fe[s] becoming present, most notably when C/O$_0$ = 0.95. If C/O$_0$ ≥ 1, TiC[s] becomes the major material of the cloud particles, but decreases as the initial C/O increases with C[s] becoming more prevalent, and indeed dominating the volume fraction at extreme initial C/O ratios (3.0, 10.0).

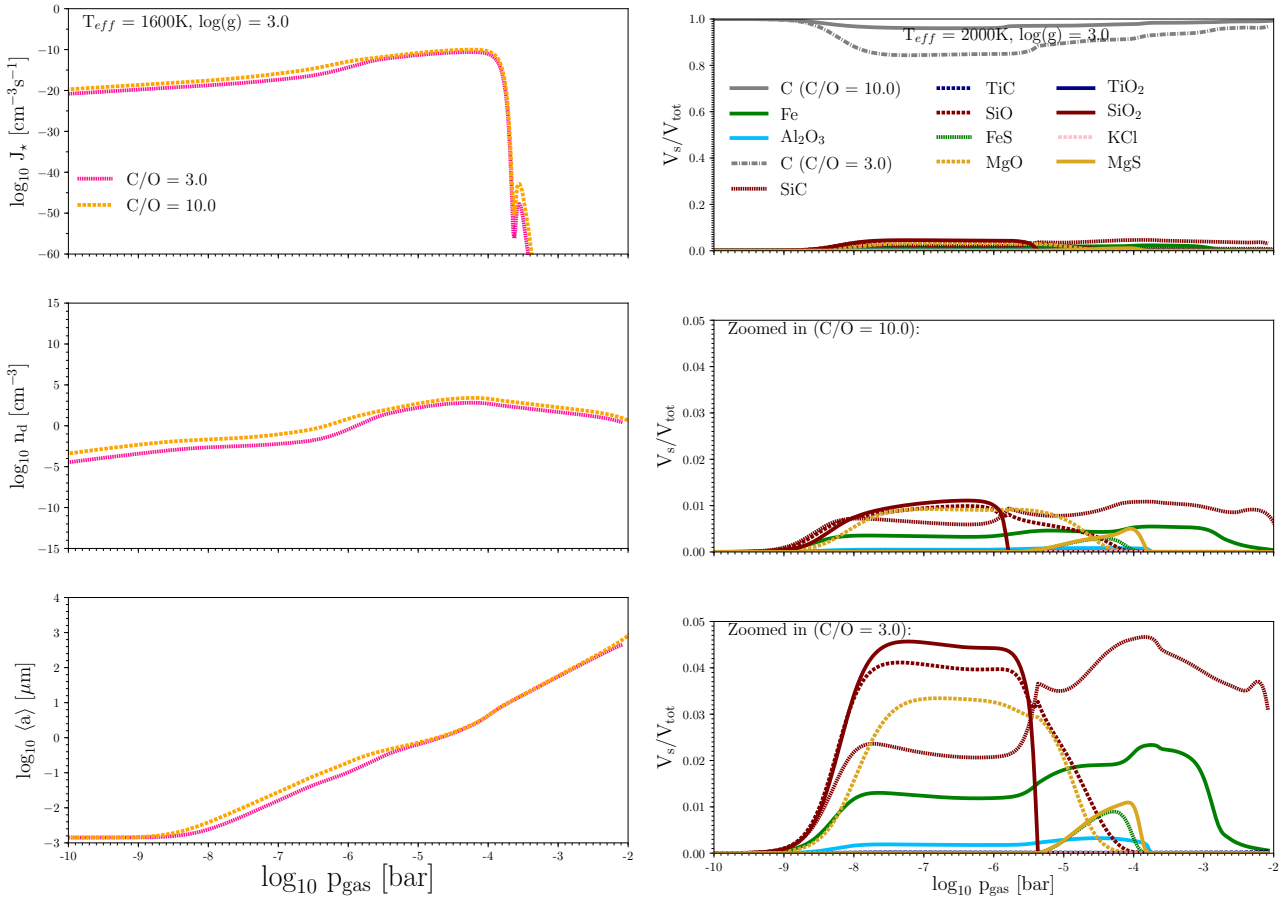

Fig. 5. *Left*: cloud structures for changing C/O = 3.0 (pink), 10.0 (orange) for a prescribed DRIFT-PHOENIX ($T_{\rm gas}$, $p_{\rm gas}$) structure for a giant gas planet with $T_{\rm eff}$ = 2000 K, log(g) = 3.0, initial solar element abundances. *1st panel*: nucleation rate log J_* [cm^{-3} s^{-1}], *2nd panel:* cloud particle number density log $n_{\rm d}$ [cm^{-3}], and *3rd panel*: mean cloud particle radius log$\langle a \rangle$ [μm]. *Right*: *1st panel* changing material composition, $V_s/V_{\rm tot}$ [%] (relative volume fractions of solid species s) of the cloud particles for C/O ratios = 3.0 and 10.0.

3.4. Extreme C/O$_0$

We briefly examine the cloud structure and cloud composition of atmospheres extremely rich in carbon (C/O$_0$ = 3.0, 10.0). Only such extremely carbon-rich cases produce cloud or dust particles that are made almost entirely of carbon with only very little inclusion of other materials. These results are not only of interest for planetary atmosphere research but also for modeling the ISM enrichment through AGB star winds and the enrichment of the early universe due to SNe ejecta (e.g., Mashian & Loeb 2016). In particular the in situ formation of carbon-rich planets in the early universe as by-products of CEMP stars would occur at C/O$_0$ > 10.0 (Table 1 in Mashian & Loeb 2016).

Cloud structure: Figure 5 illustrates the cloud structure in extremely carbon-rich environments. The general trends of the nucleation rate (top panel), number density (second panel), and average grain size (third panel) appear to be very similar to the trends presented for C/O$_0$ = 1.1 and 1.5 in Fig. 1, although they are somewhat larger. This is expected for the nucleation rate (higher C/O ratio equates to a larger abundance of potential seed material in gaseous C) and hence the number density. The increased grain size is again caused by the increased abundance of growth material (here: carbon). It is interesting to note that increasing the C/O$_0$ ratio dramatically from 3.0 to 10.0 does not cause dramatic changes in the cloud structure, as one order of magnitude in the grain number density in the upper half of the cloud layer is the most notable difference.

Dust composition: a dramatic effect of the increased initial C/O ratio from 3.0 to 10.0 is seen however, in Fig. 5 (right). This figure demonstrates the dust composition in the extreme carbon-rich environments. At C/O$_0$ = 10.0, no less than roughly 95% of the dust volume is carbon at any point in the cloud layer, with SiO[s], SiO$_2$[s], SiC[s], and MgO[s] making up only 1% of the remaining fraction each in the lower and middle cloud (2nd panel of Fig. 5 r.h.s.; this is a zoom-in of the 1st panel). In contrast, when the C/O$_0$ = 3.0 the carbon fraction drops to roughly 85% of the total volume in the upper middle portion of the cloud, with Panel 3 showing SiO$_2$[s] and SiO[s] fractions around four times greater than present in C/O$_0$ = 10.0 and a MgO[s] fraction roughly three times as large. In the lower portions of the cloud, these fractions evaporate and are replaced by a SiC[s] and Fe[s] with each roughly a four times greater fraction than their equivalent fractions in the C/O$_0$ = 10.0 case.

4. Element depletion

The element abundances, $\epsilon_{\rm x}$, determine the chemical composition of the atmospheric gas from which the cloud particles form. The cloud formation processes reduce the element abundances through nucleation and surface growth or enrich these elements

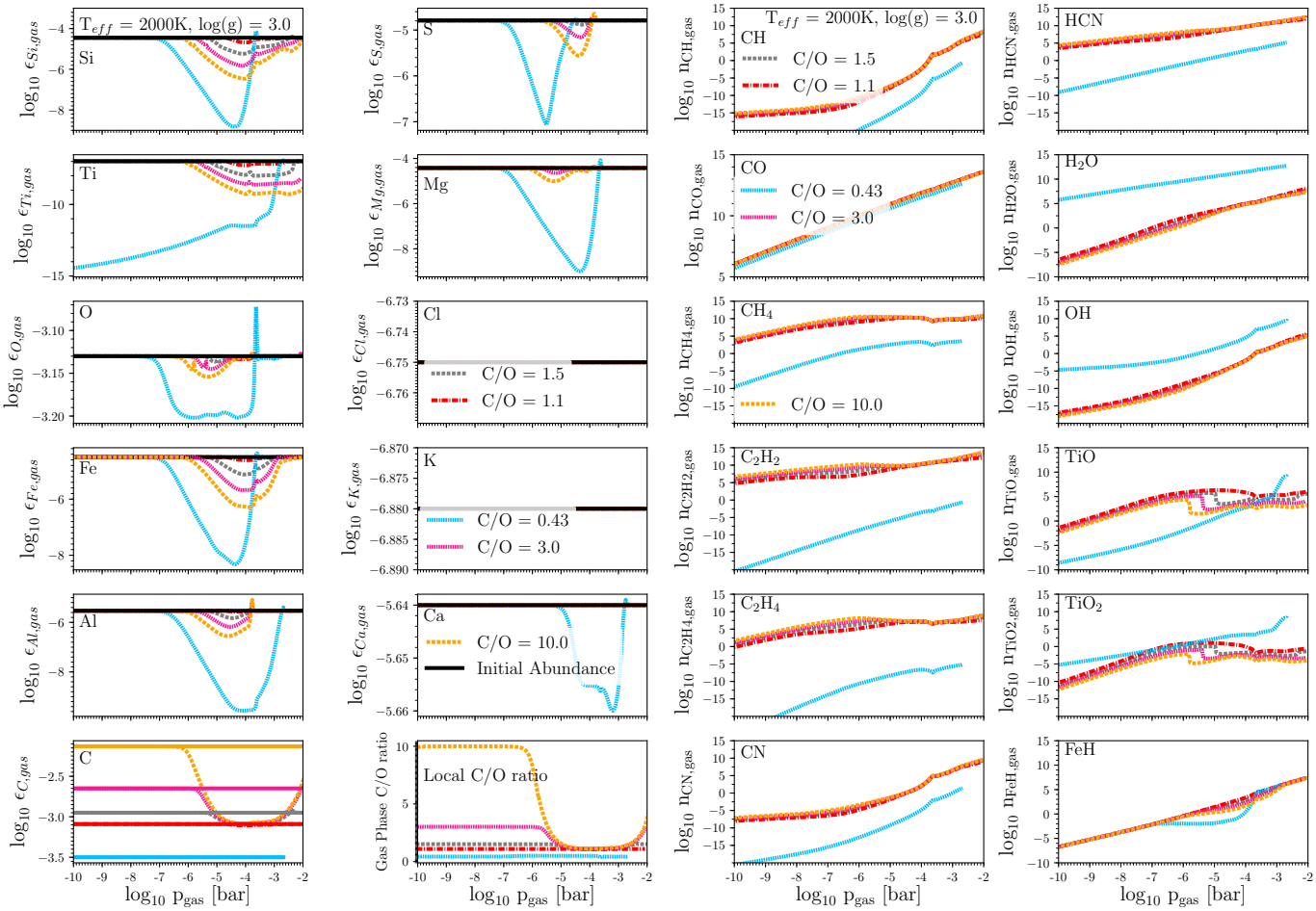

Fig. 6. Remaining gas-phase chemistry after cloud formation: *Left*: depleted gas element abundances after cloud formation. *Right*: molecular abundances of a selected number of species to demonstrate the differences between the oxygen-rich (blue) and carbon-rich cases. The underlaying atmosphere model is the same as in Fig. 1 with $T_{\rm eff}$ = 2000 K, $\log(g) = 3.0$ and initial solar abundances with the carbon adjusted according to the C/O ratio listed.

where evaporation occurs. We therefore study the effect of a changing C/O_0 ratio on the element abundances remaining in the gas phase after the cloud particles have formed. All element abundances are plotted in comparison to the initial solar element abundances (straight solid line) with ϵ_C adjusted according to the C/O_0 ratio. Figure 6 (left, panels depict different ranges) show how differently the elements that participate in cloud formation are depleted if the $C/O_0 = 0.43$, 1.0, 1.1, 1.5.

The largest element depletion, by orders of magnitude, for the C/O_0 ratios studied here occurs for $C/O_0 = 0.43$, i.e., in the oxygen-rich case for Si, S, Ti, Mg, O, Fe, Al, and Ca. This is supported by our findings that a considerably larger number of cloud particles compose a cloud in an oxygen-rich compared to a carbon-rich cloud atmosphere, despite remaining smaller in size. The element depletion generally becomes smaller when approaching $C/O_0 = 1.0$ (compare $C/O_0 = 1.5$, 1.1, 1.0), and increases again when the case is clearly carbon rich such as for $C/O_0 = 1.5$. The largest carbon-depletion occurs for $C/O_0 = 1.5$ as now the carbon contributes the largest volume fraction until its thermal stability limit near to bottom of the cloud. Somewhat more cloud particles form for $C/O_0 = 1.5$ compared to $C/O_0 = 1.1$, which does affect the element depletion (see Fig. 1).

Different nucleation species affect the chemical feedback on the gas phase differently. Ti is the most depleted element in the oxygen-rich case, while carbon remains moderately abundant even at very high C/O_0. An interesting case occurs in the transition regime where $C/O_0 \approx 1.0$. Here, carbon-nucleation alone is insufficient in describing element depletion. Both, TiO_2 nucleation and the simultaneous consideration of carbon and TiO_2 ($C + TiO_2$) produce very similar results, except that the simultaneous C + TiO_2 nucleation leads to a somewhat stronger depletion of Ti and to less depletion of Fe, Al, S, and Ca. These differences are, however, very small.

K and Cl are not depleted for any of the C/O_0 ratios considered. This is in agreement with that KCl material volume fraction ≈0 in Figs. 1 and 2 (both r.h.s.). KCl is therefore a super inefficient growth species in the temperature regime represented by our $T_{\rm eff}$ = 2000 K, $\log(g) = 3.0$ (oxygen rich, initial solar element abundances) DRIFT-PHOENIX model atmosphere.

4.1. The local C/O ratio

The last row in Fig. 6 (left panel right column) also shows the local, height-dependent C/O ratio for different global, initial C/O_0 ratios = 0.43, 1.0, 1.1., 1.5., 3.0, and 10.0. These results combine the depleted oxygen and the carbon abundances effected by cloud formation. We find that the carbon depletion in the carbon-rich cases makes the atmosphere locally somewhat more oxygen rich by decreasing the local C/O ratio. The largest change in the local C/O occurs for the highest value considered,

Table 1. Numerical comparison of cloud structure over range of C/O ratios.

		V_s/V_{tot}		
		Top	Middle	Bottom
C/O_0	0.43	100% TiO_2	1.2% TiO_2	1.7% TiO_2
$J_{*,max}$	4×10^{-6}		20.5% Mg_2SiO_4	97% Al_2O_3
[cm^{-3} s^{-1}]			11.2% SiO	0.4% Fe
$\langle a \rangle_{avg}$	0.13		12.6% SiO_2	0.8% $CaTiO_3$
[μm]			19.3% $MgSiO_3$	
			6.1% Al_2O_3	
			5.5% FeO	
			4.5% FeS	
			7% Fe_2O_3	
			8.9% MgO	
			5.3% MgS	
C/O_0	0.9	100% TiO_2	1.2% TiO_2	5.2% TiO_2
$J_{*,max}$	3×10^{-8}		25.1% Mg_2SiO_4	0.2% SiO
[cm^{-3} s^{-1}]			11.5% SiO	92% Al_2O_3
$\langle a \rangle_{avg}$	0.44		12.9% SiO_2	1% Fe
[μm]			18.1% $MgSiO_3$	1.5% $CaTiO_3$
			0.6% Al_2O_3	
			5.9% FeO	
			2% FeS	
			7.5% Fe_2O_3	
			9.6% MgO	
			2.1% MgS	
C/O_0	0.95	100% TiO_2	1.2% TiO_2	4.6% SiO
$J_{*,max}$	3×10^{-9}		26.1% Mg_2SiO_4	33.9% Al_2O_3
[cm^{-3} s^{-1}]			12% SiO	58.7% Fe
$\langle a \rangle_{avg}$	0.38		13.5% SiO_2	1.5% $CaTiO_3$
[μm]			18.7% $MgSiO_3$	1.2% MgO
			6.3% FeO	
			6.8% Fe_2O_3	
			9.6% MgO	
			2.1% MgS	

Notes. The top of the cloud layer corresponds to 1.43×10^{-12} bars, the middle of the cloud layer to 10^{-7} bars and the bottom of the cloud layer to between 1.37×10^{-3} bars and 8.64×10^{-2} bars, depending on the C/O ratio.

which is $C/O_0 = 10$. All carbon-rich cases approach approximately the same local $C/O \approx 1.0$ in the atmospheric region with the strongest carbon depletion. This is also apparent from ϵ_C in the same figure (left column). The evaporation of the carbon at the cloud bottom leads to a small increase of the C/O ratio

Table 2. Numerical comparison of cloud structure over range of C/O ratios.

		V_s/V_{tot}		
		Top	Middle	Bottom
C/O_0	1.0	100% C	1.3% TiO_2	0.5% C
$J_{*,max}$	7×10^{-12}		27.2% Mg_2SiO_4	99.3% TiC
[cm^{-3} s^{-1}]			12.5% SiO	0.1% Fe
$\langle a \rangle_{avg}$	4.47		14.1% SiO_2	
[μm]			3.8% Fe	
			19.5% $MgSiO_3$	
			10.9% MgO	
			5.6% C	
			4% SiC	
C/O_0	1.05	100% C	1.4% TiO_2	4.3% C
$J_{*,max}$	2×10^{-13}		25.5% Mg_2SiO_4	0.3% SiC
[cm^{-3} s^{-1}]			11.8% SiO	95.4% TiC
$\langle a \rangle_{avg}$	5.88		3.8% SiO_2	0.8% Fe
[μm]			18.3% $MgSiO_3$	
			10.1% MgO	
			11.3% C	
			4.2% SiC	
C/O_0	1.1	100% C	5.9% Fe	4.3% C
$J_{*,max}$	8×10^{-13}		0.5% Al_2O_3	0.3% SiC
[cm^{-3} s^{-1}]			26.7% C	95.4% TiC
a_{avg}	13.31		8.3% SiC	
[μm]			19.7% SiO	
			16.3% MgO	
			22.1% SiO_2	
C/O_0	1.5	100% C	3.1% Fe	21.2% C
$J_{*,max}$	7×10^{-12}		0.2% Al_2O_3	0.5% SiC
[cm^{-3} s^{-1}]			59.9% C	78.3% TiC
$\langle a \rangle_{avg}$	31.60		5.5% SiC	
[μm]			10.8% SiO	
			8.5% MgO	
			11.8% SiO_2	
C/O_0	3.0	100% C	1.2% Fe	96.8% C
$J_{*,max}$	2×10^{-11}		84.4% C	3.1% SiC
[cm^{-3} s^{-1}]			2.2% SiC	
$\langle a \rangle_{avg}$	36.56		4.1% SiO	
[μm]			3.3% MgO	
			4.5% SiO_2	
C/O_0	10.0	100% C	0.3% Fe	99.5% C
$J_{*,max}$	1×10^{-10}		96% C	0.4% SiC
[cm^{-3} s^{-1}]			0.6% SiC	
$\langle a \rangle_{avg}$	67.38		0.9% SiO	
[μm]			0.9% MgO	
			1.1% SiO_2	

Notes. The top of the cloud layer corresponds to 1.43×10^{-12} bars, the middle of the cloud layer to 10^{-7} bars and the bottom of the cloud layer to between 1.37×10^{-3} bars and 8.64×10^{-2} bars, depending on the C/O ratio.

above the initial value that is strongest for the highest C/O_0. As the oxygen abundance decreases by cloud formation in oxygen-rich atmospheres, the local C/O ratio increases somewhat. This has been discussed in Bilger et al. (2013) for different global parameters ($T_{\rm eff}$, $\log(g)$, [M/H]). Helling et al. (2014) demonstrated that oxygen depletion for a global $C/O = 0.99$ can lead to a substantial increase in C/O locally.

5. The abundances of gas-phase molecules

Oxygen-rich gases (including CO and H_2O) and carbon-rich gases (incl. CO, CH_4) are dominated by different molecules (Fig. 6). CO blocks oxygen in carbon-rich gases and carbon in oxygen-rich gases, unless the gas pressure is too high. In cool atmospheres with high densities, CH_4 becomes the most important carbon-binding species. Figure 6 (right) shows that CO blocking works well in the case studied here.

Figure 6 further demonstrates the abundance of a number of selected molecules after cloud formation has reduced the element abundances as shown in Fig. 6: H_2O is the dominating oxygen-binding molecule regardless of oxygen depletion. TiO drops substantially in abundance and would produce a false positive of a carbon-rich atmosphere due to the strong Ti depletion as result of cloud formation. The initial low Ti element abundance make TiO a good tracer for chemical effects on the atmospheric oxygen reservoir: TiO also traces the oxygen depletion in the center of the cloud in carbon-rich atmospheres (yellow to red lines), and the oxygen enrichment at the bottom of the cloud in the oxygen-rich case (blue lines). The TiO abundance returns to undepleted oxygen-rich values only when cloud particle evaporation has caused a considerable oxygen enrichment (see peak, blue line, on ϵ_O on left in Fig. 6). FeH, as one example for metal-hydrate molecules, reflects the Fe depletion in the oxygen-rich case. Fe[s] contributes only with $1 \ldots 3\%$ to the particle volume in the carbon-rich cases, hence, causing only little effect on the FeH abundance. All other hydrates that bind elements, which participate in cloud formation, show a similar behavior. Metal hydrates can therefore appear relatively stronger in a spectrum of a cloud-forming atmosphere.

A carbon-rich atmosphere is dominated by more complex molecules like HCN, CH_4, and CO, with small carbohydrates like C_2H_2 and C_2H_4 increasing in abundance with increasing carbon content. Even though C_2H_2 is more abundant than CN, CN has a larger absorption cross section and would therefore be easier picked up from a spectrum (see Fig. 9 in Helling et al. 2000).

6. Concluding remarks

We present the first cloud formation model that is applicable to 1D atmosphere simulations of carbon-rich planetary objects. Carbon-rich atmospheres of planets might indicate a particular chemical niche during the chemical evolution of a protoplanetary disk. Carbon planets, however, have also been suggested to form in the early universe as by-products of Pop II stars. However, observing those might only be possible if they, for example, emerge as nearby free-floating planets.

Clouds forming in carbon-rich atmospheres differ from their oxygen-rich counterparts in that fewer cloud particles form that grow to larger sizes and a large fraction of their material is made of carbon. Similar to the oxygen-rich case, the cloud properties change with height and the cloud particles are made of a mix of materials. Cloud particles can only be nearly homogeneous if the initial C/O ratio is ~10.0. Such high C/O ratios are so far predicted from low-metallicity theoretical AGB star models or for carbon-enhanced metal-poor stars.

When cloud particles rain (gravitational settle) into the deeper atmosphere, they encounter increasing densities and increasing temperatures. The increasing densities increase the thermal stability of the materials and speed up the growth process because of an increase of surface reactions. The temperature, however, allows the material to restructure into well-ordered matrices as pointed out by Helling & Rietmeijer (2009). Therefore, amorphous materials such as carbon can turn into its crystalline counterpart, i.e., into diamonds, which would cause a drastic change of optical properties during the cloud formation process. Clouds on super-carbon-rich planets may therefore effect the spectral appearance far less than in their oxygen-rich counterparts.

Carbon dust has been studied in great detail to understand the enrichment of the ISM by stellar winds on the AGB which yield the precurser for star and planet formation. Andersen et al. (1999) demonstrate that the extinction coefficient of amorphous carbon has no spectral feature for $\lambda > 0.3\ \mu$m (their Fig. 1), the exact value depending somewhat on the data source used. Silicon carbide (SiC[s]) is another material that forms from AGB star winds that has been identify from a broad emission feature $11 \ldots 11.5\ \mu$m (Sect. 3.3 in Andersen et al. 1999; Suh 2000). However, aromatic 3.3 μm PAH feature and the aliphatic subfeatures in the range of $3.4 \ldots 3.6\ \mu$m were observed in the ISM and interpreted as a mix of HAC and PAH absorption representing small dust grains (Gadallah et al. 2013). The transmission spectrum of the hot Jupiter WASP-12b is almost completely flat. The optical slope appears considerably shallower compared to HD 189744b (Sing et al. 2016). While it is almost impossible that pure carbon can condense in any oxygen-rich atmosphere based on an equilibrium gas-phase chemistry composition, carbon and carbonaceous material appears in abundance if $C/O > 1$. It might therefore be thinkable that either i) the atmosphere of WASP-12b is indeed carbon rich as the detection of HCN and C_2H_2 would suggest; ii) the original atmosphere was nearly carbon rich and an efficient cloud formation tipped it over to the carbon-rich regime (such as in Fig. 9 in Helling et al. 2014); or iii) external irradiation (e.g., cosmic rays) drives a strong ion-neutral chemistry, which leads to the emergence of larger carbohydrate molecules (Rimmer et al. 2014).

Acknowledgements. We highlight financial support of the European Community under the FP7 by an ERC starting grant number 257431. A summer scholarship for D.T. provided by the Royal Astronomical Society is highly acknowledged.

References

Abia, C., Domínguez, I., Gallino, R., et al. 2003, PASA, 20, 314
Ali-Dib, M., Mousis, O., Petit, J.-M., & Lunine, J. I. 2014, ApJ, 785, 125
Andersen, A. C., Loidl, R., & Höfner, S. 1999, A&A, 349, 243
Barnes, R., Deitrick, R., Luger, R., et al. 2016, ArXiv e-prints [arXiv:1608.06919]
Bilger, C., Rimmer, P., & Helling, C. 2013, MNRAS, 435, 1888
Eistrup, C., Walsh, C., & van Dishoeck, E. F. 2016, A&A, 595, A83
Fleischer, A. J., Gauger, A., & Sedlmayr, E. 1992, A&A, 266, 321
Fortney, J. J. 2012, ApJ, 747, L27
Fortney J. J., Robinson T. D., Domagal-Goldman S., et al. 2016, ArXiv e-prints [arXiv:1602.06305]
Gadallah, K. A. K., Mutschke, H., & Jäger, C. 2013, A&A, 554, A12
Helling C., & Casewell, S. 2014, A&ARv, 22, 80
Helling, C., & Fomins, A. 2013, Phil. Trans. R. Soc. London Ser. A, 371, 20110581
Helling, C., & Rietmeijer, F. J. M. 2009, Int. J. Astrobiol., 8, 3

Helling, C., & Woitke, P. 2006, A&A, 455, 325
Helling, C., Dehn, M., Woitke, P., & Hauschildt, P. H. 2008, ApJ, 675, L105
Helling, C., Jorgensen, U. G., Plez, B., & Johnson, H. R. 1996, A&A, 315, 194
Helling, C., Winters, J. M., & Sedlmayr, E. 2000, A&A, 358, 651
Helling, C., Woitke P., Rimmer P. B., et al. 2014, Life, 4, 142
Helling, C., Woitke, P., & Thi, W.-F. 2008, A&A, 485, 547
Jeong, K. S., Chang, C., Sedlmayr, E., & Sülzle, D. 2000, J. Phys. B At. Mol. Phys., 33, 3417
Jeong, K. S., Winters, J. M., & Sedlmayr, E. 1999, in Asymptotic Giant Branch Stars of Dust formation in oxygen-rich circumstellar shells around long–period variables, eds. T. Le Bertre, A. Lebre, & C. Waelkens, IAU Symp., 191, 233
Jura, M., Dufour, P., Xu, S., et al. 2015, ApJ, 799, 109
Kreidberg, L., Line, M. R., Bean, J. L., et al. 2015, ApJ, 814, 66
Lee, G., Helling, C., Giles, H., & Bromley, S. T. 2015, A&A, 575, A11
Madhusudhan, N., Harrington, J., Stevenson, K. B., et al. 2011, Nature, 469, 64
Mashian, N., & Loeb, A. 2016, MNRAS, 460, 2482
Mattsson, L., Wahlin, R., & Höfner, S. 2010, A&A, 509, A14
Morley, C. V., Fortney, J. J., Marley, M. S., et al. 2012, ApJ, 756, 172
Oppenheimer, B. R., Baranec, C., Beichman, C., et al. 2013, ApJ, 768, 24
Rimmer, P. B., Helling, C., & Bilger, C. 2014, Int. J. Astrobiol., 13, 173
Schröder, K.-P., Winters, J. M., Arndt, T. U., & Sedlmayr, E. 1998, A&A, 335, L9
Sharp, C. M., & Huebner, W. F. 1990, ApJS, 72, 417
Sing, D. K., Fortney, J. J., Nikolov, N., et al. 2016, Nature, 529, 59
Suh, K.-W. 2000, MNRAS, 315, 740
Tsiaras, A., Rocchetto, M., Waldmann, I. P., et al. 2016, ApJ, 820, 99
Winters, J. M., Le Bertre, T., Jeong, K. S., Nyman, L.-Å., & Epchtein, N. 2003, A&A, 409, 715
Witte, S., Helling, C., & Hauschildt, P. H. 2009, A&A, 506, 1367
Wittkowski, M., Chiavassa, A., & Freytag, B. 2016, A&A, 587, A12
Woitke, P. 2006, A&A, 452, 537
Woitke, P., & Helling, C. 2003, A&A, 399, 297
Woitke, P., & Helling, C. 2004, A&A, 414, 335
Woitke, P., Kamp, I., & Thi, W.-F. 2009, A&A, 501, 383
Woitke, P., Min, M., Pinte, C., et al. 2016, A&A, 586, A103
Yang, J., Cowan, N. B., & Abbot, D. S. 2013, ApJ, 771, L45

Appendix A: Surface growth reactions and vapor pressure data

The sets of surface reaction that are provided here have been applied to model oxygen-rich and carbon-rich cloud particle growth by gas-surface reactions as outlined in Helling et al. (2008). The cloud particle growth in a clearly oxygen-rich environment (e.g., C/O = 0.43) is described by the surface reaction listed in Table 1 in Helling et al. (2008) plus those listed in Table A.2 in the present paper, adding to a total of 73 surface reactions. For the carbon-rich case, we use 84 surface reactions, which include the reactions for TiO_2[s], SiO_2[s], SiO[s], Fe[s], FeS[s], MgO[s], and Al_2O_3[s] (32 reactions) as listed in Table 1 in Helling et al. (2008) plus those given in Table A.3.

Table A.1 contains the vapor pressure data used for the materials that were added to our cloud model; C[s], MgS[s], TiC[s], SiC[s], KCl[s]). C[s], TiC[s], and SiC[s] are fits to the JANAF table (1986). MgS[s] is taken from Sharp & Huebner (1990), and KCl[s] from Eq. (18) in Morley et al. (2012).

Table A.1. Monomer volumes $V_{0,s}$ of solid materials and fit coefficients c_i for the calculation of saturation vapor pressures and difference Gibbs free energies.

Condensate	$V_{0,s}$ [10^{-23} cm^3]	c_1	c_2	c_3	c_4	c_5	Fit of	
C[s]	1.002	1.01428E+6	−7.23043E+5	1.63039E02	−1.75890E-3	9.97416E08	ln p_{sat}	(*)
MgS[s]	3.296	−7.93442E+4	−1.83584E+5	6.33920	−8.89360E-4	0.0	$\Delta G'$	(**)
	8.89360E-5	−4.20876E-9	$\Delta G'$	(**)				
TiC[s]	2.018	1.11878E+5	−1.37612E+6	3.20666E+2	−4.63379E-3	1.85306E-7	$\Delta G'$	(*)
SiC[s]	2.074	6.73337E+5	−1.24381E+6	3.21779E+2	−4.54405E-3	2.69711E-7	$\Delta G'$	(*)
KCl[s]	6.227	7.611 – 11382.0/T_{gas}					log p_{sat}	(***)

References. (*): performed for this paper from JANAF tables (1986) – (**): Sharp & Huebner (1990), (***) Morley et al. (2012).

Table A.2. Oxygen-rich cloud formation.

Index r	Solid s	Surface reaction	Key species
61	KCl[s]	KCl → KCl[s]	KCl
62	sylvite	KOH + HCl → KCl[s] + H_2O	min{KOH, HCl}
63		HK + HCl → KCl[s] + H_2	min{HK, HCl}
64		KOH + CaCl → KCl[s] + CaOH	min{KOH, CaCl}
65	MgS[s]	MgS → MgS[s]	MgS
66	niningerite	2 MgH + 2 FeS → 2 MgS[s] + H_2 + 2 Fe	min{MgH, FeS}
67		2 MgH + 2 H_2S → 2 MgS[s] + 3 H_2	min{MgH, H_2S}
68		2 MgOH + 2 H_2S → 2 MgS[s] + 2 H_2O + 1 H_2	min{MgOH, H_2S}
69		MgOH + CaS → MgS[s] + CaOH	min{MgOH, CaS}
70		MgO + CS → MgS[s] + CO	min{MgO, CS}
71		2 MgH + 2 CS → 2 MgS[s] + H_2 + 2 C	min{MgH, CS}
72		MgO + H_2S → MgS[s] + H_2O	min{MgO, H_2S}
73		Mg + H_2S → MgS[s] + H_2	min{Mg, H_2S}

Notes. Dust growth surface reactions for a oxygen-rich environment in addition to those listed in Table 1 in Helling et al. (2008). This set of 73 reactions is applied for all oxygen-rich models in the present paper.

Table A.3. Carbon-rich cloud formation: Dust growth surface reactions for a carbon-rich environment in addition to those listed in Table 1 in Helling et al. (2008) for TiO_2[s], SiO_2[s], SiO[s], Fe[s], FeS[s], MgO[s], and Al_2O_3[s] (32 reactions).

Index r	Solid s	Surface reaction	Key species
33	C[s]	$C \rightarrow C[s]$	C
34	carbon	$C_2 \rightarrow 2\ C[s]$	C_2
35		$C_3 \rightarrow 3\ C[s]$	C_3
36		$2\ C_2H \rightarrow 4\ C[s] + H_2$	C_2H
37		$C_2H_2 \rightarrow 2\ C[s] + H_2$	C_2H_2
38		$CH_4 \rightarrow C[s] + 2\ H_2$	CH_4
39	TiC[s]	$Ti + C \rightarrow TiC[s]$	min{Ti, C}
40	titanium-	$2\ Ti + C_2 \rightarrow 2\ TiC[s]$	min{Ti, C_2}
41	carbide	$3\ Ti + C_3 \rightarrow 3\ TiC[s]$	min{Ti, C_3}
42		$4\ Ti + 2\ C_2H \rightarrow 4\ TiC[s] + H_2$	min{Ti, C_2H}
43		$2\ Ti + C_2H_2 \rightarrow 2\ TiC[s] + H_2$	min{Ti, C_2H_2}
44		$Ti + CH_4 \rightarrow TiC[s] + 2\ H_2$	min{Ti, CH_4}
45		$TiC \rightarrow TiC[s]$	TiC
46		$TiS + C + H_2 \rightarrow TiC[s] + H_2S$	min{TiS, C}
47		$2\ TiS + C_2 + 2\ H_2 \rightarrow 2\ TiC[s] + 2\ H_2S$	min{TiS, C_2}
48		$3\ TiS + C_3 + 3\ H_2 \rightarrow 3\ TiC[s] + 3\ H_2S$	min{TiS, C_3}
49		$4\ TiS + 2\ C_2H + 3\ H_2 \rightarrow 4\ TiC[s] + 4\ H_2S$	min{TiS, C_2H}
50		$2\ TiS + C_2H_2 + H_2 \rightarrow 2\ TiC[s] + 2\ H_2S$	min{TiS, C_2H_2}
51		$TiS + CH_4 + H_2 \rightarrow TiC[s] + H_2S$	min{TiS, CH_4}
52		$TiC_2 \rightarrow TiC[s] + C$	TiC_2
53	SiC[s]	$Si + C \rightarrow SiC[s]$	min{Si, C}
54	silicon-	$2\ Si + C_2 \rightarrow 2\ SiC[s]$	min{Si, C_2}
55	carbide	$3\ Si + C_3 \rightarrow 3\ SiC[s]$	min{Si, C_3}
56		$4\ Si + 2\ C_2H \rightarrow 4\ SiC[s] + H_2$	min{Si, C_2H}
57		$2\ Si + C_2H_2 \rightarrow 2\ SiC[s] + H_2$	min{Si, C_2H_2}
58		$Si + CH_4 \rightarrow SiC[s] + 2\ H_2$	min{Si, CH_4}
59		$SiC \rightarrow SiC[s]$	SiC
60		$SiS + C + H_2 \rightarrow SiC[s] + H_2S$	min{SiS, C}
61		$2\ SiS + C_2 + 2\ H_2 \rightarrow 2\ SiC[s] + 2\ H_2S$	min{SiS, C_2}
62		$3\ SiS + C_3 + 3\ H_2 \rightarrow 3\ SiC[s] + 3\ H_2S$	min{SiS, C_3}
63		$4\ SiS + 2\ C_2H + 3\ H_2 \rightarrow 4\ SiC[s] + 4\ H_2S$	min{SiS, C_2H}
64		$2\ SiS + C_2H_2 + H_2 \rightarrow 2\ SiC[s] + 2\ H_2S$	min{SiS, C_2H_2}
65		$SiS + CH_4 + H_2 \rightarrow SiC[s] + H_2S$	min{SiS, CH_4}
66		$Si_2C \rightarrow SiC[s] + Si$	Si_2C
67		$SiC_2 \rightarrow SiC[s] + C$	SiC_2
68		$SiH_4 + C \rightarrow SiC[s] + 2\ H_2$	min{SiH_4, C}
69		$2\ SiH_4 + C_2 \rightarrow 2\ SiC[s] + 4\ H_2$	min{SiH_4, C_2}
70		$3\ SiH_4 + C_3 \rightarrow 3\ SiC[s] + 6\ H_2$	min{SiH_4, C_3}
71		$3\ SiH_4 + 2\ C_2H \rightarrow 4\ SiC[s] + 9\ H_2$	min{SiH_4, C_2H}
72		$2\ SiH_4 + C_2H_2 \rightarrow 2\ SiC[s] + 5\ H_2$	min{SiH_4, C_2H_2}
73		$SiH_4 + CH_4 \rightarrow SiC[s] + 4\ H_2$	min{SiH_4, CH_4}
74	KCl[s]	$KCl \rightarrow KCl[s]$	KCl
75	sylvite	$HK + HCl \rightarrow KCl[s] + H_2$	min{KH, HCl}
76		$2\ CKN + 2\ H_2O + CaCl_2 \rightarrow 2\ KCl[s] + 2\ C + N_2 + Ca(OH)_2 + H_2$	min{CKN, $CaCl_2$}
77	MgS[s]	$MgS \rightarrow MgS[s]$	MgS
78	niningerite	$2\ MgH + 2\ H_2S \rightarrow 2\ MgS[s] + 3\ H_2$	min{MgH, H_2S}
79		$2\ MgOH + 2\ H_2S \rightarrow 2\ MgS[s] + 2\ H_2O + H_2$	min{MgOH, H_2S}
80		$MgOH + CaS \rightarrow MgS[s] + CaOH$	min{MgOH, CaS}
81		$2\ MgN + 2\ H_2S \rightarrow 2\ MgS[s] + 2\ H_2 + N_2$	min{MgN, H_2S}
82		$2\ MgH + 2\ CS \rightarrow 2\ MgS[s] + H_2 + 2\ C$	min{MgH, CS}
83		$2\ MgOH + 2\ TiS \rightarrow 2\ MgS[s] + H_2 + 2\ TiO$	min{MgOH, TiS}
84		$Mg + H_2S \rightarrow MgS[s] + H_2$	min{Mg, H_2S}

Notes. This set of 84 reactions is applied for all carbon-rich models.

Appendix B: More detailed results

Figure B.1 provides more detailed results of the cloud structures for the initial C/O ratios 0.43, 1.1, and 1.5 the results of which were presented in Sect. 3. The plots in Fig. B.1 have the same setup as in our previous publication to allow for a sensible comparison of cloud structures forming in different atmospheric conditions. The plots allow for a more detailed comparison between the oxygen-rich and the carbon-rich cloud formation.

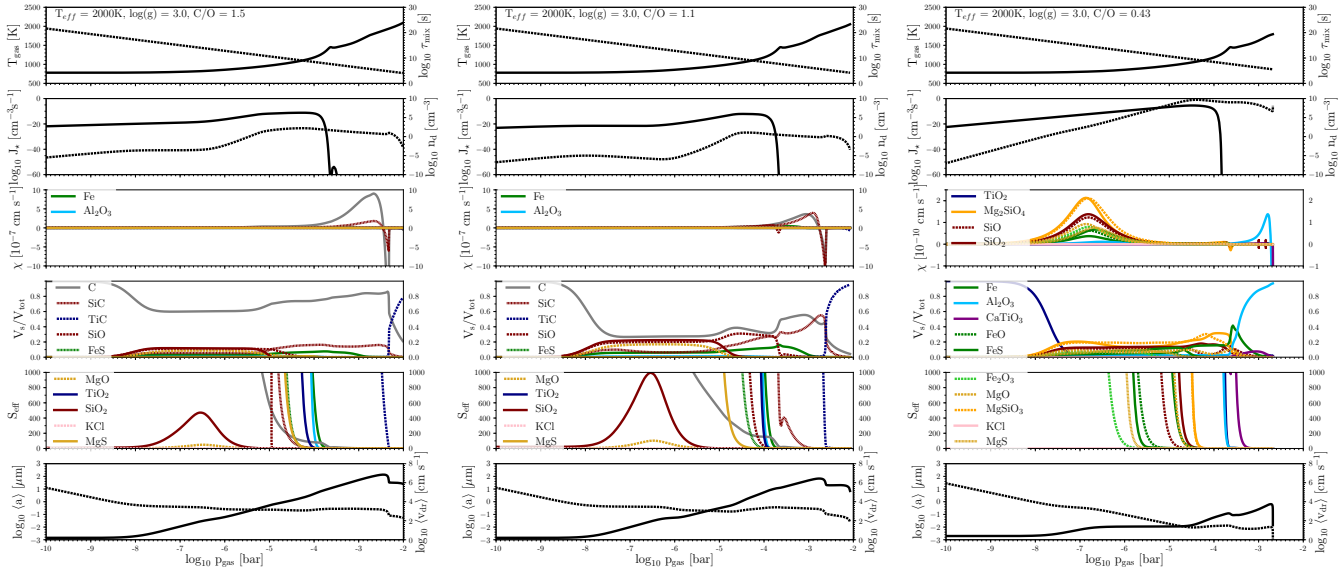

Fig. B.1. Detailed information about the cloud structure forming in an atmospheric gas with initial C/O ratios of 0.43, 1.1, 1.5 and a prescribed DRIFT-PHOENIX atmosphere profile for $T_{\rm eff}$ = 2000 K and $\log(g) = 3.0$. *1st row*: local gas temperature $T_{\rm gas}$ [K] (solid, *left*), mixing timescale $\tau_{\rm mix}$ [s] (dashed, *right*); *2nd row:* seed formation rate J_* [cm^{-3} s^{-1}] (solid, *left*), number density of cloud particles $n_{\rm d}$ [cm^{-3}] (*right*, dashed), *3rd row:* net growth velocity for individual materials s; *4th row*: volume fraction $V_s/V_{\rm tot}$ for material s; *5th row*: effective supersaturation ratio $S_{\rm eff}$ for each material s; *6th row:* mean cloud particles radius $\langle a \rangle$ [μm], drift velocity $v_{\rm drift}$ [cm s^{-1}] with respect to the local $\langle a \rangle$. The color code is the same for all panels. All quantities are plotted vs. the local gas pressure $p_{\rm gas}$ [bar].